The role of Manganese in CoMnO$_x$ Catalysts for Selective Fischer-Tropsch Synthesis

Hao Chen[1], Zan Lian[2], Xiao Zhao[3,4], Jiawei Wan[3,4], Priscilla F. Pieters[5], Judit Oliver Meseguer[1], Ji Yang[3], Elzbieta Pach[3], Sophie Carenco[3], Laureline Treps[3], Nikos Liakakos[3], Yu Shan[1,4], Virginia Altoe[6], Ed Wong[6], Zengqing Zhuo[7], Feipeng Yang[7], Ji Su[3], Jinghua Guo[7], Monika Blum[7], Lapidus Saul H[8], Adrian Hunt[9], Iradwikanari Waluyo[9], Hirohito Ogasawara[10], Haimei Zheng[3,4], Peidong Yang[1,4,5], Alexis T. Bell[1,11], Núria López[2], Miquel Salmeron[1,3,4]*

[1]Chemical Sciences Division, Lawrence Berkeley National Laboratory, Berkeley, California 94720, United States

[2]Institute of Chemical Research of Catalonia (ICIQ-CERCA), Barcelona Institute of Science and Technology (BIST), Av. Països Catalans 16, 43007 Tarragona, Spain

[3]Materials Science Division, Lawrence Berkeley National Laboratory, Berkeley, California 94720, United States

[4]Department of Materials Science and Engineering, University of California, Berkeley, California 94720, United States

[5]Department of Chemistry, University of California, Berkeley, California 94720, United States

[6]Molecular Foundry, Lawrence Berkeley National Laboratory, Berkeley, California 94720, United States

[7]Advanced Light Source, Lawrence Berkeley National Laboratory, Berkeley, CA, 94720, United States

[8]Advanced Photon Source, Argonne National Laboratory, Lemont, IL, United States

[9]National Synchrotron Light Source II, Brookhaven National Laboratory, Upton, NY 23 11973, United States

[10]SLAC National Accelerator Laboratory, 2575 Sand Hill Road, Menlo Park, California 94025, United States

[11]Department of Chemical and Biomolecular Engineering, University of California, Berkeley, California 94720, United States

*Corresponding author. E-mail: mbsalmeron@lbl.gov

Abstract

The origin of the high selectivity of cobalt-manganese oxide ($CoMnO_x$) catalysts in the Fischer−Tropsch synthesis (FTs) reaction towards long-chain hydrocarbon products was investigated using model systems of $CoMnO_x$ in the form of crystalline nanoparticles and amorphous thin films where Co and Mn are intimately mixed rather than separated in two phases. Using ambient pressure X-ray photoelectron spectroscopy and X-ray adsorption spectroscopy, the chemical structure of the catalyst and adsorbed species were determined under reaction conditions. We found that the catalytically active phase contains an outer layer enriched in metallic Co relative to the bulk. Molecular CO adsorbs on Co^0 sites, where it dissociates by reaction with H_2 to form cobalt carbide and CH_x species. The concentration of CH_x increases rapidly with exposure to CO/H_2 syngas on the $CoMnO_x$ catalyst, while no such increase was observed in the absence of Mn. Density Functional Theory (DFT) simulations indicate that MnO acts as a reservoir of H atoms bound to the basic O sites, which makes it less accessible to CH_x moieties, thus hindering chain termination to form short chain hydrocarbons. In contrast, the increasing concentration of CH_x moieties helps chain growth.

1. Main

The Fischer−Tropsch synthesis (FTs) reaction converts syngas (CO and H_2) to hydrocarbons, with cobalt (Co) being one of the most efficient catalysts [1-3]. The most desirable reaction products are long-chain hydrocarbons rather than methane [4]. This has been shown to be enhanced when Co is promoted by manganese (Mn), which shifts the products towards C_{5+} and longer hydrocarbons [5-17]. It has also been shown that formation of alcohols and aldehydes can be favored on CoMn catalyst [16, 18-20]. More recently, cobalt carbides formed following CO dissociation have been proposed to be active for direct conversion of syngas to lower olefins [21, 22]. Up to now, however, the nature of the active sites, reaction steps, and intermediate species present under reaction conditions is hampered by the heterogeneity of powder catalysts, which makes atomic-level investigations difficult.

In this study we used two model catalysts to reduce the complexity of powder catalysts: one in the form of crystalline nanoparticles (NPs) of $CoMnO_x$ [23, 24], the other in the form of amorphous films of $CoMnO_x$ with thickness of 100 nm deposited on silicon wafers, and of 10 nm-thick films on silicon nitride (SiN_x) TEM grids. An important feature of our catalysts is that in both cases Co and Mn are intimately mixed at the atomic scale, rather than in the form of Co particles in contact with MnO_2. Our model catalysts facilitate structural and spectroscopic studies under reaction conditions, providing new insights into the nature of the active sites and the special role of Mn. We used ambient pressure XPS (APXPS), and X-ray Absorption Spectroscopy (XAS) in-situ to determine the chemical structure of the catalysts and the nature of the species formed by exposure to CO and H_2 reactants. We show that the presence of Mn substantially enhances the formation of CH_x species under CO+H_2 syngas, which explains the higher selectivity for long-chain hydrocarbon products. DFT simulation identifies the role of MnO_x, which controls the chemical potential of oxygen and H, promoting higher concentration of active species and C-C coupling reactions while reducing the C-H coupling termination step, due to the restricted supply of H.

2. Preparation of model catalysts

Crystalline nanoparticles of mixed Co and Mn oxide ($CoMnO_x$ NPs) were synthesized by hot injection of $Co_2(CO)_8$ and $Mn_2(CO)_{10}$ into a solution of octyl-ether in the presence of oleic

acid.[25-27] High-resolution scanning transmission electron microscopy (STEM) results show that the CoMnO$_x$ NPs are crystals of ~10 nm diameter (**Fig.1a**). Two atomic plane distances of 0.248 nm and 0.217 nm are observed, consistent with the (-111) and (002) lattice spacings of CoO (**Fig.1b**), indicating that they are solid solutions of Mn in the CoO matrix. The Co:Mn ratio in the nanocrystals can be finely tuned by changing the feeding ratio of the precursors. The initial oxidation state of CoMn is due to reaction with oleic acid and exposure to air. The 10 nm thin films of CoMnO$_x$ were prepared by sequential evaporation of Co and Mn onto a Si wafer and onto SiN$_x$ TEM windows. Both CoMnO$_x$ NPs and films were activated by oxidation at 300 °C under 1 bar of O$_2$ and subsequent reduction at 450 °C under 1 bar of H$_2$. High-angle-annular-dark-field (HAADF), STEM, and energy-dispersive X-ray spectroscopy (EDS) images of the activated CoMnO$_x$ NPs, and CoMnO$_x$ thin films are shown in **Fig.1c–1h**, showing that in all cases Co and Mn are and homogeneously mixed at the sub-nm scale.
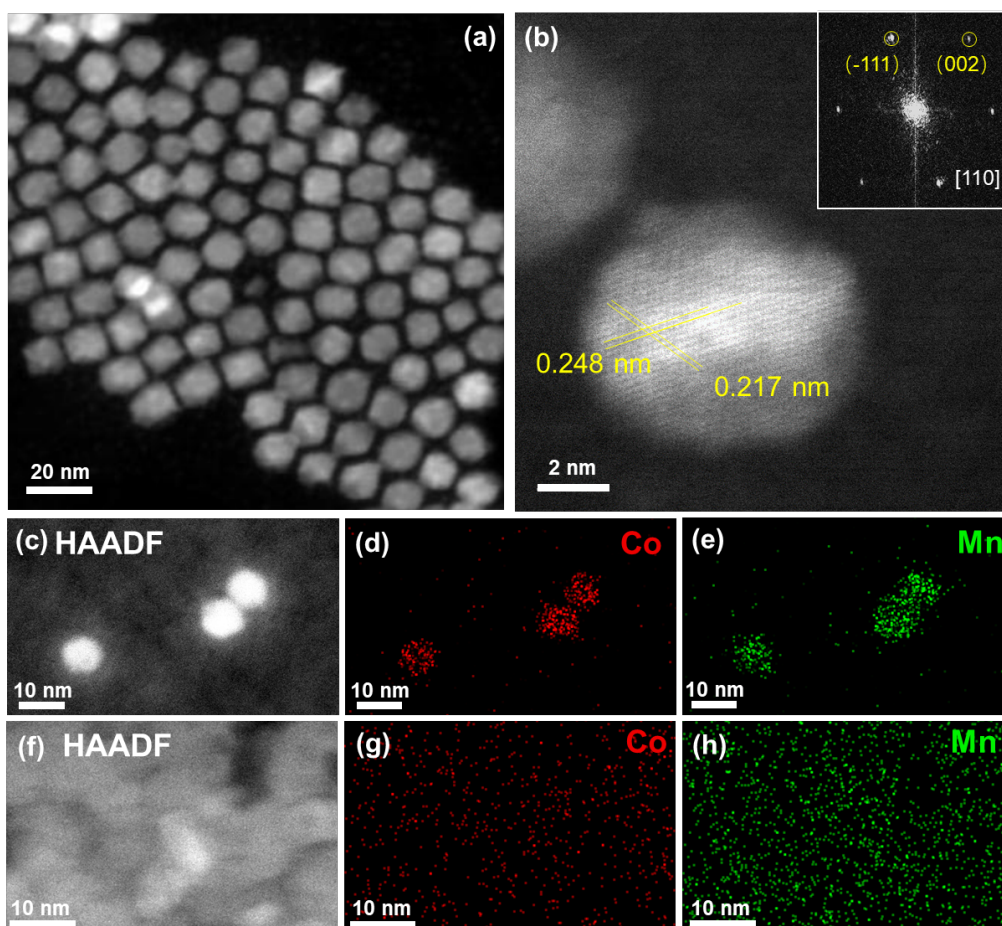

Fig.1 (a) STEM-HAADF images of as-synthesized CoMnO$_x$ crystal NPs; **(b)** High resolution STEM image of a CoMnO$_x$ NP, with the inset showing its FFT pattern; STEM-HAADF image and EDS maps of **(c-e)** CoMnO$_x$ NPs and

(f-h) 10 nm thick amorphous $CoMnO_x$ film grown on a SiN_x membrane after activation. The EDS images show that in both cases Co and Mn are intimately mixed at the sub-nanometer scale.

3. Catalytic activity measurements.

The FTs activity of the activated $CoMnO_x$ NPs model catalysts was measured using a fixed-bed reactor described in the Methods section. The results for two different Co/Mn composition ratios are shown in **Fig.2**. Product distributions from pure Co supported on Al_2O_3, and the prediction from the Anderson–Schulz–Flory (ASF) model for a chain growth probability α of 0.5 are shown for comparison [1]. Under steady state (10% CO conversion, 220 °C, 1 bar, H_2/CO ratio of 2), the $CoMnO_x$ nano-catalysts displayed a higher selectivity for production of hydrocarbons with chain lengths ≥ 5 carbon unit (C_{5+}: 48%) versus methane (CH_4: 20%), than that of the Co/Al_2O_3 catalyst (C_{5+}: 25%; CH_4: 38%). The product distribution on these $CoMnO_x$ NPs obeys the ASF distribution with α = 0.76, in agreement with previous results [8, 17]. The larger α value indicates enhanced chain growth/propagation rate versus chain termination. These results show that our model $CoMnO_x$ NPs perform similarly to traditional powder-form catalysts in terms of product distribution, with enhanced percentage of hydrocarbon chains lengths of more than 5 carbons units.
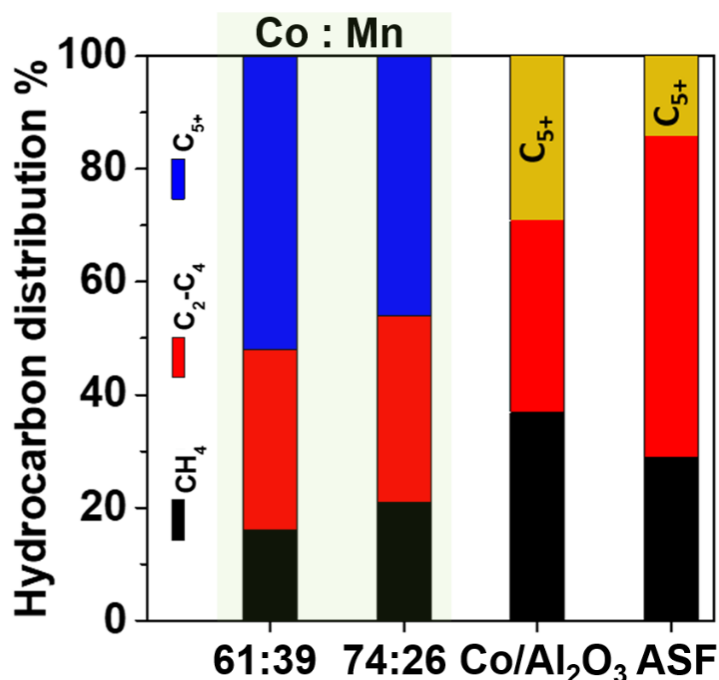

Fig.2 Catalytic performance of $CoMnO_x$ NPs for the FTs reaction. Hydrocarbon distribution over $CoMnO_x$ NPs for two Co:Mn composition ratios, and for a pure Co catalyst. The prediction from the ASF model for a chain growth probability of 0.5 is also shown. Methane product selectivity (black bars) is highest in the absence of Mn.

4. Spectroscopic characterization.

4.1. Catalyst structure after activation.

APXPS characterization results from $CoMnO_x$ NPs under 100 mTorr of O_2 at 300 °C and under subsequent 100 mTorr H_2 at 500 °C, are shown in **Fig.3a**, **3b**. A depth profile of the Co and Mn composition was obtained from the intensity ratios of the Co 3p and Mn 3p peaks in the XP spectra fitted with red/green traces for the $3p_{3/2}$, and with blue/orange traces for the $3p_{1/2}$ spin-orbit components, using photon energies of 770 eV and 270 eV (top and bottom spectra in (a) and in (b) respectively), which generate photoelectrons of ~700 eV and ~200 eV energies with mean free paths of ~1.2 nm and ~0.6 nm, respectively. We will refer to these as 'near' and 'top' surface regions, respectively (illustrated in **Fig.3c, 3d**). For a $CoMnO_x$ NPs with Co:Mn ratio of 2.76:1 (from ICP), the peak intensities after oxidation indicate a Co:Mn ratio of 1:1 for the top surface region, and 2:1 for the near surface region, indicating surface enrichment of Mn **(Fig.3c)**. The oxidation process resulted in a mixture of Co^{2+}, Co^{3+}, Mn^{2+}, and Mn^{3+}, in chemical states as in Co_3O_4 and Mn_3O_4, respectively **(Fig.S1a-b)**. The reduction under 100 mTorr of H_2 at 300 °C brought no appreciable changes in surface composition **(Fig.S2a)**, and only chemical changes of Co and Mn, which were both reduced to the 2+ state **(Fig.S2b, 2c)**. However, when the temperature was raised to 450 °C and above, the surface composition changed significantly, as indicated by the increase of XPS peak intensity ratio **(Fig.3b)**, which now corresponds to a Co/Mn ratio of 6 in the near surface region and 2.5 in the top surface region, respectively **(Fig.3c)**. EDS maps **(Fig.S1c, Fig.1c-1e)** demonstrate the preservation of the $CoMnO_x$ bulk structure during oxidation/reduction pretreatment, indicating that the pretreatments mostly affect the redistribution of Co and Mn in the surface region. The higher temperature reduction, however, changed the oxidation state of Co from 2+ to metallic Co while Mn remained in the 2+ state, as can be seen in the XAS of the samples along with reference spectra from Co, CoO, Mn_2O_3, and MnO_2 **(Fig.3e, 3f)**. This is also shown in the APXPS results discussed below. The two-step reduction pattern is similar to that reported for $CoMnO_x$ catalysts prepared by co-impregnation [6, 7].
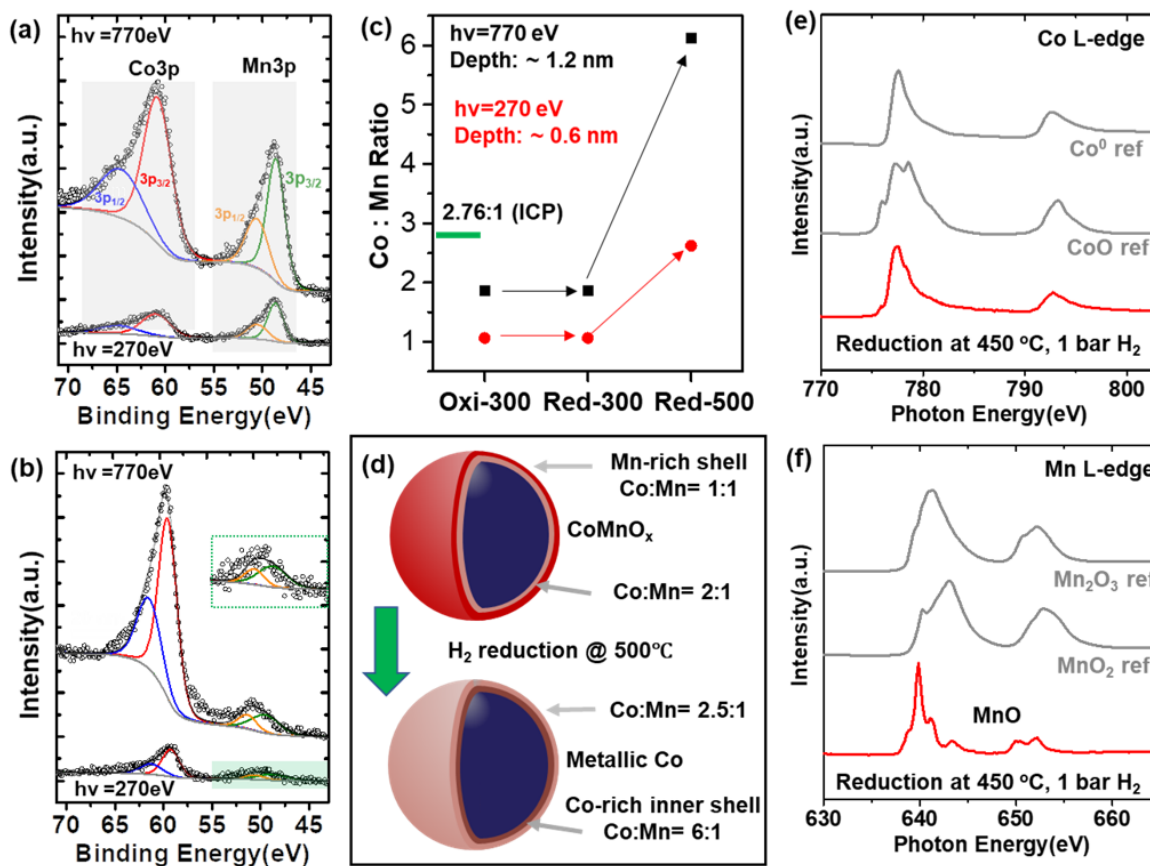
Fig.3 Surface evolution of CoMnO$_x$ NPs under catalytic conditions. Co3p and Mn3p XP spectra: **(a)** under 100mTorr O$_2$ at 300 °C. **(b)** under 100mTorr H$_2$ at 500 °C. Two photon energies, 770eV and 270 eV (top and bottom in each panel) were used to obtain a depth distribution profile, based on the different mean-free paths of 1.2 and 0.6 nm respectively of the corresponding photoelectrons. The colored curves are fitting peaks for the 3p$_{1/2}$ and 3p$_{3/2}$ components for each Co and Mn. The inset in the green box shows an expanded view of the Mn 3p XPS (hv =270 eV) region in (**b**). **(c)** Co: Mn ratio in the top surface region (~0.6nm, red points) and near surface region (~1.2nm, black points) after the oxidation and reduction treatments. **(d)** illustrations of the composition distribution of CoMnO$_x$ NPs before and after 100 mTorr H$_2$ reduction at 500 °C. **(e-f)** L-edge XAS from CoMnO$_x$ NPs after activation by reduction in 1 bar of H$_2$ at 450 °C for Co and for Mn (red), with measured spectra of known compounds (gray) for comparison. The top surface of the activated catalyst contains Co^0 and Mn^{2+} in a 2.5:1 ratio.

4.2. Surface species formed by CO adsorption on CoMnO$_x$, MnO, and CoO films.

The nature of the species formed on the catalysts after exposure to CO and its reaction with H$_2$ was studied by APXPS on CoMnO$_x$, MnO, and CoO films, with the results shown in **Fig.4**. The films were deposited side-by-side on a Si wafer for comparison of their structure under the same

conditions and same oxidation/reduction procedures as for the $CoMnO_x$ NPs. The bottom gray spectrum corresponds to the activated $CoMnO_x$ film in ultra-high vacuum (UHV). The spectrum above it, acquired under 100mTorr of CO at room temperature (RT), shows C 1s peaks at ~ 292 eV from gas phase CO (fitted with a red peak), carbonate at ~289.6 eV (green), chemisorbed molecular CO at ~286.0 eV (blue), CH_x at ~284.8 eV (orange), and cobalt carbide at ~283.5 eV (black). On pure Co (middle spectrum), apart from the gas phase peak (at slightly different energy due to differences in sample work function [28]), a molecularly adsorbed CO peak at 286 eV is visible together with a small carbide peak at ~283.5 eV. On pure MnO (top spectrum), only carbonate (at ~289 eV) and CH_x (at ~285 eV) are formed, the latter likely by contamination from background gases. From these results we conclude that on activated $CoMnO_x$, molecular CO species adsorb molecularly on the Co^0 sites while it forms carbonates on MnO.
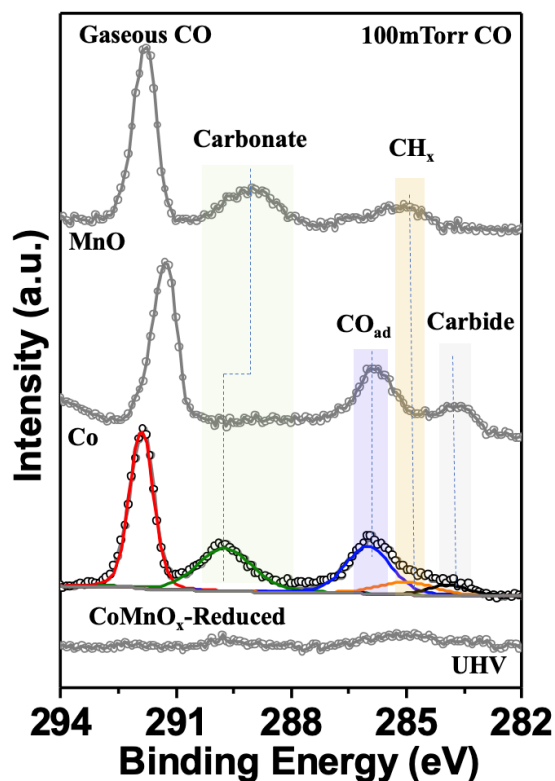

Fig.4 Surface structure of $CoMnO_x$ thin film from APXPS. From bottom: Spectrum in UHV after activation, showing that the $CoMnO_x$ surface is virtually clean (gray curve); above, spectrum after introducing 100mTorr of CO, with the red, green, blue, orange and grey fitting curves for gas CO at ~292 eV (with small changes due to different sample work function), carbonate (~289.6 eV), chemisorbed (CO_{ad}

~286.0 eV), CH_x (~284.8 eV), and carbide (~283.5 eV) species. On pure Co, only chemisorbed CO and some carbides are formed; on pure MnO (top), only peaks from carbonate and CH_x adsorbates are present.

4.3. Reactions between CO and H_2 on CoMnO$_x$ NPs, and on CoMnO$_x$, MnO, CoO thin films.

We then studied the reaction between CO and H_2 on both CoMnO$_x$ NPs and thin films. The reaction cell used for the NPs is closed by a 100 nm thick Si_3N_4 window that separates the volume inside, filled with 1 bar of reaction gases, from the beamline chamber. The CoMnO$_x$ NPs, supported on a gold foil, were first reduced by exposure to 1 bar 10% H_2/Ar at 450 °C (heated using an 805 nm IR laser via an optical fiber from the back) and then cooled to reaction temperature (schematic in **Fig. 5a**).[25, 29] All XAS spectra were recorded in the Total Electron Yield (TEY) detection mode, measuring the sample to ground current [25]. Due to the short mean free path of the emitted electrons, the TEY technique is surface sensitive to a depth of few nm. The O K-edge XAS of the sample after reduction before CO introduction, is shown by the black curve in **Fig.5b.** The peak at ~531 eV arises from lattice oxygen in MnO [25] [30], and the broad peak at ~540 eV from excitations from O1s core level electrons to unoccupied σ^* bands of MnO [30]. After exposure to CO, which adsorbs molecularly only on the Co^0 sites of the CoMnO$_x$ surface, an intense peak at ~534 eV is observed corresponding to the excitation of O1s level electrons to the empty π^* antibonding orbital of CO [25] (**Fig.5b, red curve**). On MnO however, CO forms only carbonates as shown in **Fig.4**, which also contribute to the 534 eV peak [30]. After flowing H_2 at 2.5 mL/min at 1 bar for 12 min with the sample at 150 °C, the intensity of the peak at ~534 eV dropped significantly as a function of time (**Fig.5c**) due to the H_2-assisted CO dissociation reaction [25]. The remaining peak, after all molecular CO has been dissociated (**Fig.5b,** blue curve), corresponds to unreacted carbonates on MnO$_x$ [12]. **Fig.5d** shows the evolution of the π^* peak intensity as a function of reaction time for 3 temperatures: RT, 100 °C, and 150 °C. The linear relationship suggests a constant reaction rate. An Arrhenius plot of the rate, **Fig.5e**, gives an activation energy of ~28 kJ/mol, a value substantially smaller than that of the typical FTs reaction (80 kJ/mol)[8], indicating that the H_2-assisted CO dissociation is not the rate-limiting step among the various reaction steps on the Co-MnO surface.

The chemical state of CoMnO$_x$ NPs under reaction conditions was also followed by APXPS. After reduction by exposure to 100 mTorr H_2 at 500 °C (**Fig.6a**, black curve), the spectra show that most of the Co atoms in the top surface region (~ 4.6 Å), are in the metallic state, while within the same

depth (**Fig.6b**) Mn remains in the 2+ state. Following exposure of the reduced sample to 100 mTorr of CO at 220 °C, a fraction of the metallic cobalt oxidized to CoO due to dissociation of CO [26], as indicated by the increased shoulder intensity at ~781.3 eV from Co^{2+} (**Fig.6a,** red curve). Under 300 mTorr of syngas (CO:H_2 =1:2), the oxide peak increased substantially and became the dominant peak (**Fig.6a**, blue curve). The increased oxidation is the result of both H_2- assisted CO dissociation and thermal dissociation of CO, also confirmed by the increased area of the Co^{2+} peak in the Co L-edge XAS (**Fig.S3a**). During this period, no significant changes in the MnO were observed (**Fig.6b and Fig.S3b**). More important, a depth profile using the XPS peaks of Co 3p and Mn 3p (**Fig.S3c-3d**) demonstrate that under syngas reaction conditions at 220 °C, the compositions of top surface and near surface region remain unchanged during reaction, indicating the stability of the Co-MnO structure and that oxidized Co from the H_2-assisted CO dissociation is subsequently reduced by H_2.
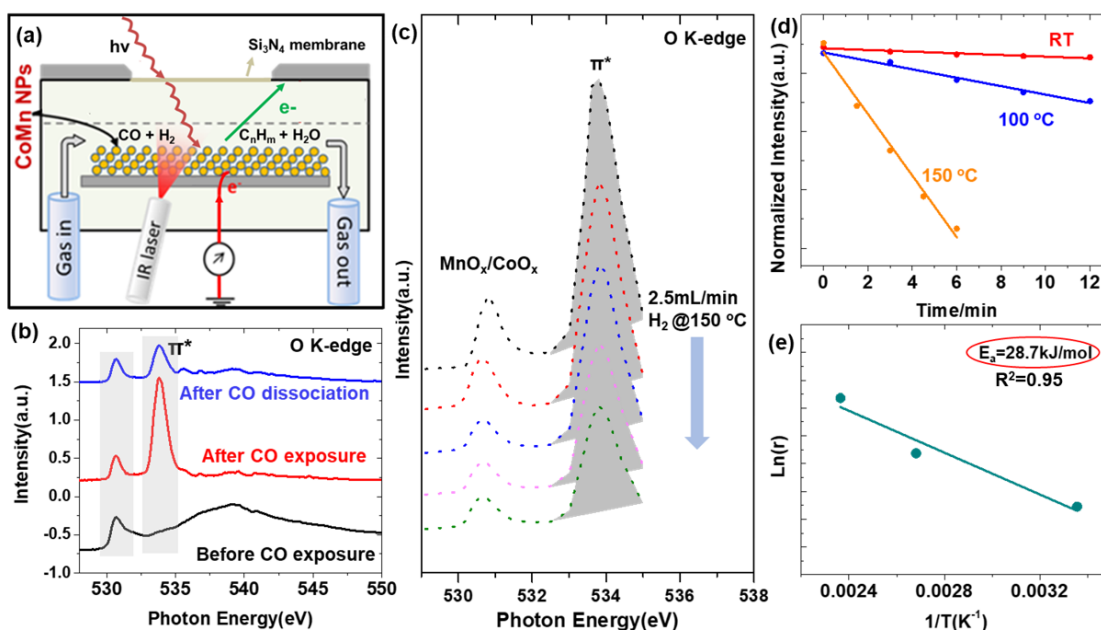

Fig.5. Reactions between CO and H_2 on CoMnO$_x$ crystal NPs. (a) Schematic illustration of the reaction cell used for in-situ reaction studies using TEY-XAS. The yellow circles represent CoMnO$_x$ NPs on a gold foil covering a Si wafer. **(b)** O K-edge XAS of CoMnO$_x$ before (black), after CO exposure (red), and after H_2 introduction (blue). The peak a 531 eV is due to lattice O in CoMnO$_x$. The peak at 534 eV corresponds to a transition of electrons from the O1s level of CO to the antibonding orbital (π*) upon adsorption of X-rays. This peak has contributions from both molecular CO, adsorbed on Co^0, and from carbonates formed on the MnO. The broad peak around 540 eV is due to a transition to unoccupied σ* bands in CoMnO$_x$,

which disappear due to adsorbed CO donating electrons to these orbitals. After introduction of H_2, the peak at 534 eV decreases due to H_2-assisted CO dissociation, leaving only the contribution from the carbonate species. **(c)** Time evolution of the CO π^* peak intensity under 1bar of H_2 flowing at 2.5 mL/min, at 150 °C. **(d)** Intensity of the CO π^* orbital peak as function of time for three temperatures, which measures the H_2-CO reaction rate. **(e)** Arrhenius plot from the π^* orbital peak decay rate.
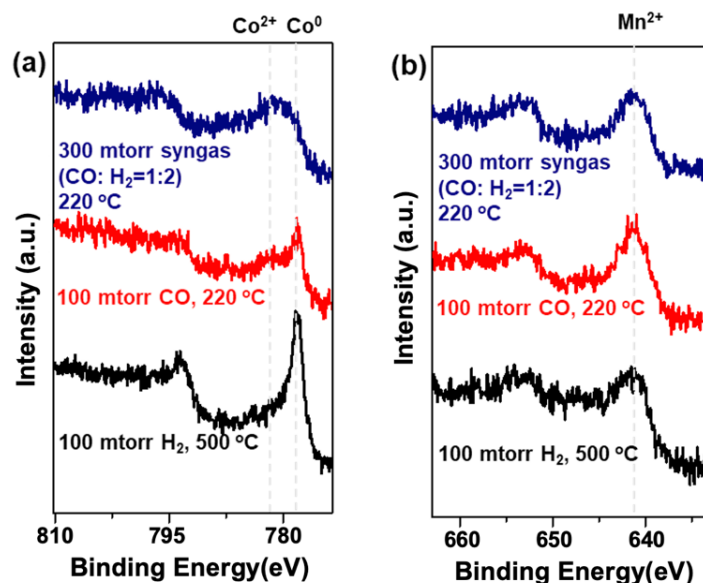
Fig.6 APXPS from CoMnO$_x$ NPs under FTs reaction conditions. (a) Co 2p and (b) Mn 2p APXPS of CoMnO$_x$ NPs acquired sequentially under 100 mTorr H_2 at 500 °C (bottom, black curve), 100 mTorr CO at 220 °C (middle, red) and 300 mTorr syngas 220 °C (upper, blue). Changes in oxidation state of Co are clearly visible, while the Mn oxidation state does not change appreciably.

The nature of the species formed on the catalyst surface during the reaction of H_2 with CO on each of the films, Co, MnO and CoMnO$_x$ is revealed by APXPS of the C 1s region shown in **Fig.7**. When the temperature was raised to 220 °C, the CO and carbonates desorb from CoMnO$_x$, while the amount of carbide increases as a result of increased CO dissociation, both thermally and by H_2-assisted reaction [25] (**Fig.7a,** black trace). After 40 min exposure to 300 mTorr of syngas (CO:H_2=1:2), CH$_x$ becomes the dominant carbonaceous species on the surface. The CH$_x$ species are stable and desorbs only when the temperature increased above 400 °C (**Fig.S4**). Their increase in concentration and higher thermal stability compared with methane suggests that they belong to longer chain intermediates formed in the chain-growth reaction [31, 32]. Most significant is the

observation that under syngas at 220°C, no significant accumulation of CH_x is observed on pure metallic Co or on MnO (**Fig.7b**). Therefore, it can be concluded that Mn^{2+} sites play a key role in the FT synthesis of C_{5+} hydrocarbons by increasing the formation rate of CH_x species, which favors chain growth by coupling of CH_x species.
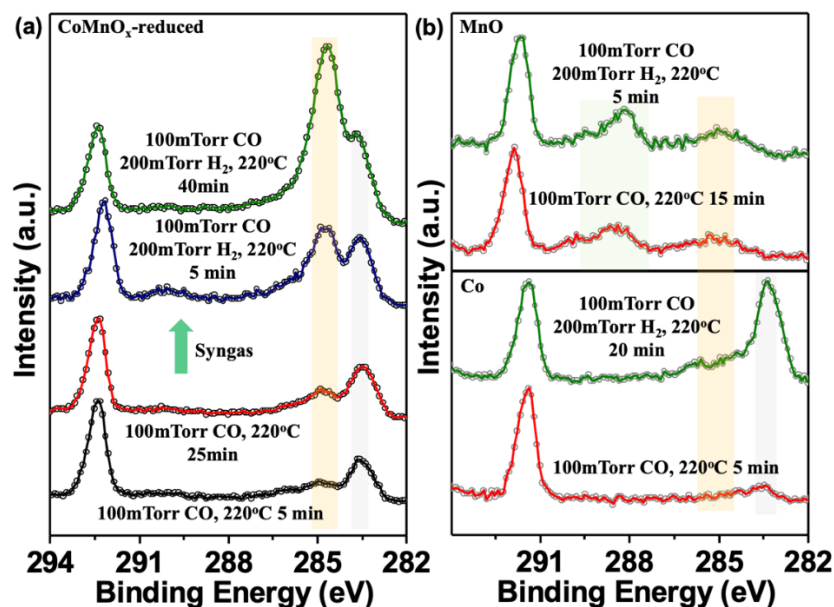

Fig.7 XPS of surface carbonaceous species on CoMnO$_x$, Co, and MnO thin films. **(a)** From bottom: activated CoMnO$_x$ under 100mTorr CO at 220°C for 5min, 25min, after under syngas (100 mTorr CO + 200 mTorr H$_2$) for 5min and 40min. The absence of the CO$_{ads}$ peak at 286 eV is due to the low CO coverage at 220°C resulting from dissociation driven by reaction with H$_2$ and desorption by equilibration with the gas phase. Most noticeable is the increase of intensity of the peak from CH$_x$ species at ~285 eV. **(b)** From bottom: Pure Co exposed to 100 mTorr CO at 220°C for 5 min (red trace), and to syngas (100 mTorr CO and 200 mTorr H$_2$) for 20 min (green trace). CO dissociation by H$_2$ produces cobalt carbide (283.5 eV) but no stable CH$_x$. Top: pure MnO exposure to the 100mTorr CO at 220°C for 15min and syngas for 5min showing negligible formation of CH$_x$ fragments.

5.4. Theoretical simulations

To better understand the origin of the high selectivity of CoMnO$_x$ catalysts towards C_{5+} hydrocarbon products in the FTs reaction, we performed DFT simulations on a model catalyst with a structure and composition compatible with the experimental data described above, i.e., Co:Mn

ratio ~ 2.5 in the topmost layer with Co in the metallic state (Co^0) and Mn with a double positive charge (Mn^{2+}). In the model, the components Co, Mn, and O are arranged in a compact structure, illustrated in **Fig.8a.** The unit cell in the topmost layer contains 12 Co atoms, 4 Mn atoms and 4 O atoms. A Bader charge analysis shows that the Mn in the model has a charge of +1.20 |e|, compared with that in MnO (+1.47 |e| for Mn in the bulk, +1.39 |e| for Mn on the surface) and in Mn_2O (+0.72 |e| for Mn in the bulk). The Mn atom in the $CoMnO_x$ model has similar oxidation state as Mn^{2+}. The average charge of all Co atoms is +0.00 |e|, and the average charge of topmost Co atoms near MnO_x is +0.07 |e|, indicating that Co is mostly metallic but slightly polarized near the MnO interface. This structure is stable against changes in oxidation state by gain or loss of oxygen atoms, as illustrated in **Fig.8a** to **8b and 8c**, respectively.
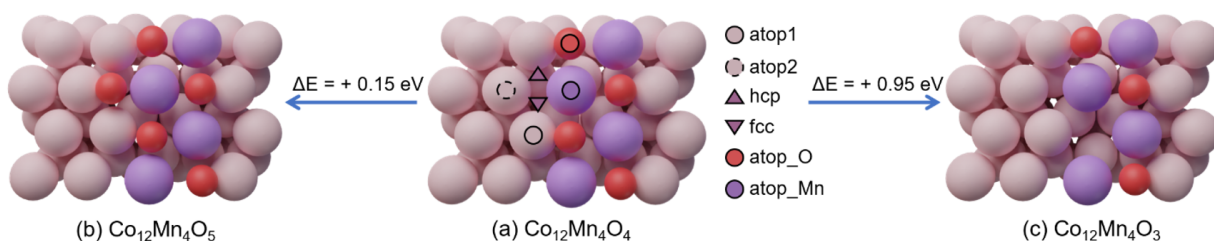

Fig.8 Structure and stability of the $CoMnO_x$ model for DFT simulations. (a) Top view of the model containing 12 Co atoms (pink), 4 Mn atoms (purple), and 4 O atoms (red) in the topmost layer. To test the stability of this model the reaction energies with H_2 and H_2O leading to (b) gain or (c) loss of O were calculated with results shown by the arrows. The sites considered for adsorption of molecular intermediates are marked in the center panel by a circle (top sites), and by triangles (3-fold hollow fcc and hcp sites).

The adsorption energies of relevant key fragments were then calculated on three simple surfaces: MnO(100), metal Co(0001), and our model $CoMnO_x$ of **Fig. 8**. The results are shown in **Table S1**. The adsorption of H, CO, CH, and CH_2 on MnO(100) was found to be weaker than on Co(0001) by 1.26 eV, 1.64 eV, 2.54 eV, and 1.86 eV, indicating that the species prefer to adsorb on Co instead of MnO. In the $CoMnO_x$ model, 6 adsorption sites near the interface are considered as shown in **Fig.8a**, which are top sites (marked by circles), and hcp and fcc 3-fold sites (marked by a down-pointing and up-pointing triangles, respectively). On $CoMnO_x$, most of the adsorbates bind preferentially to the Co sites instead of MnO sites with an adsorption energy only slightly different

from that in pure Co(0001). Some carbon fragments (CH and C_2H_2) do not adsorb on MnO_x sites in the $CoMnO_x$ model, while for CO and CH_2, the adsorption is more endothermic than on the Co sites by 1.60 eV and 1.45 eV. For H, O, and C, the adsorption is only moderately more endothermic than on the Co sites by 0.15 eV, 0.37 eV, and 0.25 eV, respectively. The diffusion of H from Co to O sites on $CoMnO_x$ is sensitive to the local interface structure: as the oxygen content changes at the interface, the energy barrier of H diffusion from Co to O sites near the interface changes from 1.47 to 0.85 eV (**Fig.S5**), indicating that the diffusion is easier on local configurations rich in oxygen.

DFT simulated energy diagrams for the reaction steps are shown in **Fig.9**. In panel (a) the continuous lines correspond to thermal CO dissociation, while the broken lines are for H_2-assisted dissociation. The black lines are for reactions on Co(0001) surface, and red lines for Co sites in the $CoMnO_x$ surface. The energy barrier of the rate determining step (RDS) for H_2-assisted dissociation on Co(0001) is 1.20 eV, while the energy barrier of CO thermal dissociation is 2.28 eV. On $CoMnO_x$, both energy barriers are decreased, the former to 0.98 eV, and the latter to 2.03 eV. Assuming the pre-exponential factor to be the same on Co(0001) and $CoMnO_x$, the reaction rate coefficient, k, on $CoMnO_x$ corresponds to two orders of magnitude (k_{CoMnOx}/k_{Co},) higher than on pure Co(0001) for a reaction temperature at ~ 220 °C. Therefore, the presence of the interface will facilitate CO dissociation and increase CHO* formation, which decomposes to form CH*.
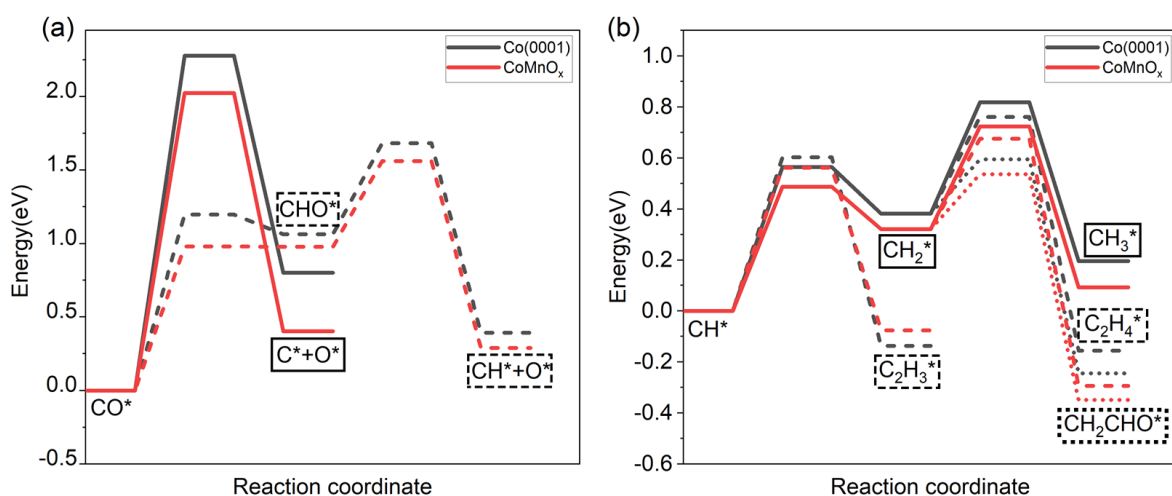

Fig 9. Energy diagrams. (a) CO dissociation reaction: Solid lines for thermally activated process; dashed lines for H_2-assisted process; The black line for pure Co; red line for $CoMnO_x$. (b) C-H and C-C bond formation reactions: Solid lines for CH*+H* reactions. Dashed lines for CH_x*+CH_2* reactions. Dotted lines

for CH$_2$*+CHO* reaction. Relative energies between elementary steps were shifted to align the initial state for energy barrier comparisons.

Reactions involving carbon fragments can proceed in two different ways (**Fig.9b**): (i) oligomerization, i.e., C-C coupling and chain growth, or (ii) termination by hydrogenation of the carbon moieties. The competition between these two processes leads to the ASF distribution. The hydrogenation of CH* and CH$_2$*, and the coupling of CH*+CH$_2$*, CH$_2$*+CH$_2$*, CH$_2$*+CHO*, were simulated to understand the effect of the MnO in the formation of C-H and C-C bonds. CH$_2$*+CHO* shows the lowest energy barrier (0.21 eV on Co(0001), 0.22 eV on CoMnO$_x$), indicating that C-C coupling can be achieved through the reaction. However, this will be controlled by the relative population of both species. Since CHO* easily dissociates into CO* and H*, the coverage of the intermediate CHO* may be low, leading to a low rate of this bimolecular reaction, therefore the reaction is not discussed in the following. In general, the C-C formation releases more energy than the C-H formation, indicating that C-C bond formation is thermodynamically favorable (**Fig.9b**, **Table S2**). Starting from CH* fragments, the energy barrier towards C-H formation (0.57 eV on Co, 0.49 eV on CoMnO$_x$) is lower than the C-C formation (0.60 eV on Co(0001), 0.56 eV on CoMnO$_x$). However, once CH$_2$* is formed, the energy barrier for C-C coupling (0.38 eV on Co, 0.36 eV on CoMnO$_x$) is lower than C-H formation (0.44 eV on Co(0001), 0.40 eV on CoMnO$_x$), indicating that C-C formation is likely to occur with CH$_2$*.

From the simulations, the following picture of the reaction emerges (**Scheme 1**) that explains the impressive performance of CoMnO$_x$. First, syngas species adsorb on the metal and H$_2$ dissociates, with some H atoms diffusing towards the basic sites in MnO$_x$ to form hydroxyls species (**F' in panel b)**), in agreement with the appearance of a shoulder peak in the O1s spectra at ~531eV (**Fig.S6**). Once these H atoms are bound to the basic centers (O) of the CoMnO$_x$ system, they become inactive for C-H formation (E') (**Fig.S7**). The interface shows good activity in activating CO via the H$_2$-assisted pathway (A'-B'), which increases the rate and overall activity of formation of CH$_x$* species (C'). Second, chain growth steps (D') are more likely on CoMnO$_x$ compared to Co, from both coverage and energetic considerations: CH$_x$* adsorption on MnO is unfavorable and therefore, facilitating the increase of CH$_x$* coverage on Co. In addition, the barrier for C-C coupling is lower than that on pure Co, which favors chain growth. Termination step reactions are

less likely in the CoMnO$_x$ system because part of the hydrogen is bound to the oxide and also consumed to remove some of the O generated by CO dissociation. Thus, the MnO$_x$ acts as a buffer for the chemical potential of both oxygen and H under reaction conditions making them optimal to reduce side reactions.
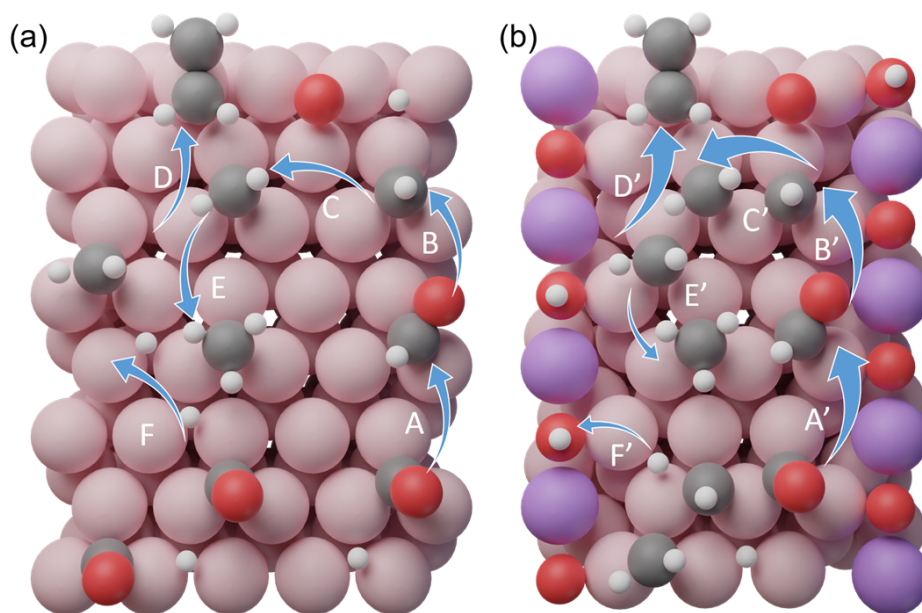
Scheme 1. The comparison of proposed mechanism of the reaction. On (a) Co(0001) and (b) CoMnO$_x$. Co in pink, Mn in purple, O in red, H in white, and C in gray. The arrows on the Co are the same size to serve as a reference. A more detailed illustration of the reaction steps is shown in **Fig.S8**.

Conclusion

By using well-defined alloy CoMnO$_x$ crystalline nanoparticles and amorphous thin films as model catalysts, where Co and Mn are not separated but mixed at the atomic scale, together with in-situ spectroscopic characterization by APXPS and XAS, and with the help of DFT calculations, we unraveled the elemental distribution of Co and Mn on the surface of the catalyst and their oxidation state, while the bulk structure stays practically unchanged. The catalytically active phase of CoMnO$_x$ under FTs reaction conditions is composed of metallic Co in contact with MnO. Our experimental data support the H$_2$-assisted CO dissociation process on the Co-MnO leading to large increases in the production of CH$_x$* intermediates much more than in pure Co, favoring chain growth in the FTs reaction. The main advantage of CoMnO$_x$ is that Mn remains always oxidized

with its O providing basic sites that bound H, thus lowering the amount available for CH_x* + H* coupling, i.e., chain termination and methane formation, while increasing the concentration of CH_x* species, which favors the C-C coupling between towards oligomerization and chain growth.

Methods

1. Preparation of model catalysts

The $CoMnO_x$ NPs were synthesized as follows: a solution of 0.5 mL of oleic acid in 15 mL of dioctyl ether was stirred under vacuum and heated to 50 C for 30 min. Next, a mixture of 205 mg of $Co_2(CO)_8$ and 117 mg of $Mn_2(CO)_{10}$ (corresponding to a feeding ratio of Co:Mn = 2:1) in 2 mL of dioctyl ether was injected in the solution. The solution was heated at 5-8 °C /min and kept at 290 °C for 1h, followed by cooling down to room temperature, with isopropanol added to precipitate the nanoparticles. The nanoparticles were purified by 2 cycles of centrifugation and redispersed in hexanes. This synthesis produced CoMn nanocrystals with diameters of ~10nm and Co:Mn composition ratio of 2.76:1, as measured by Inductively Coupled Plasma Optical Emission Spectrometry (ICP-OES).

$CoMnO_x$ thin film were prepared by sequential evaporation of Co and Mn onto a Si wafer and onto SiN_x TEM windows and heated to 300 °C under 1 bar O_2 atmosphere. Their thickness, determined from Quartz Crystal Microbalance (QCM) measurements, was 100 nm for the Si wafer substrates and 10 nm for the silicon nitride TEM windows, respectively.

2. TEM characterization

The as-prepared $CoMnO_x$ NPs were drop-cast onto a SiN_x TEM window (10 nm thickness, VWR Scientific). High resolution TEM studies were performed in an aberration corrected FEI Titan 80300 operated at 300 kV and equipped with a CEOS GmbH double hexapole aberration corrector providing angstrom level resolution in scanning imaging modes. Prior to TEM characterization, the $CoMnO_x$ NPs underwent activation, consisting of two steps: first removal of the carbon by heating in a gas flow of 20% O_2/Ar mixture, at 25mL/min, 1 bar, at 300 °C for 2 hours. The second step is a reduction in a flow of 20% or 10% H_2/He mixture at 25 mL/min, 1 bar, for 2 hours. The reduction step was done at two different temperatures of 300 °C and 450-500 °C.

3. FTs Catalytic activity measurements.

The FTs catalytic activity of the $CoMnO_x$ NPs was tested using 70 mg of NP particles supported on alumina powder by sonication with a loading of 10 wt%. The fixed-bed reactor used was heated to 450 °C with a

ramp of 5 °C /min for 2 hours in flowing H_2 and subsequently cooled to 220 °C in flowing He. After activation the gas flow or was gradually switched from He to syngas over 10 min. The syngas was composed of H_2, CO (H_2/CO at a ratio of 2:1), and 7% Ar (Praxair, 99.999% purity) used as an internal standard. The catalyst temperature was measured using a K-type thermocouple positioned in the bed center. An Agilent 6890N gas chromatograph was used to monitor the chemical composition of the reactor effluent. The gas chromatograph was equipped with a capillary column connected to a flame ionization detector to measure the hydrocarbon products, and a packed column connected to a thermal conductivity detector for measuring H_2, Ar, and CO.

4. In-situ APXPS and TEY-XAS characterization

For in-situ APXPS and TEY-XAS experiments, the $CoMnO_x$ NPs were drop-cast onto an Au foil and activated as indicated above. The APXPS acquired in beamline 9.3.2 of the Advanced Light Source (ALS) at the Lawrence Berkeley National Laboratory (LBNL). XAS experiments were performed using a gas cell in beamline 8.0.1.4 of the ALS with an energy resolution of 0.2 eV for the Co L-edge, Mn L-edge and O K-edge. The reaction cell is closed by a 100 nm thick Si_3N_4 window that separates the volume inside, filled with 1 bar of reaction gases, from the high vacuum beamline chamber.[25, 29] The $CoMnO_x$ NPs, supported on the Au foil, were heated using an 805 nm IR laser via an optical fiber that illuminates the sample from the back. Copper gas lines were used to introduce the CO and H_2 reactants with Cu carbonyl traps kept at ~ 240 ℃ to remove any carbonyls present. All measurements were conducted under flowing gas conditions.

Data availability

The model system, structures of adsorption and reaction are available in ioChem-BD database [33] (DOI: 10.19061/iochem-bd-6-272). (Embargo link for peer-review: https://iochem-bd.bsc.es/browse/review-collection/100/305486/61c2ee93b4e0e48443131a59)

References

1. Zhou, W., et al., *New horizon in C1 chemistry: breaking the selectivity limitation in transformation of syngas and hydrogenation of CO2 into hydrocarbon chemicals and fuels.* Chem Soc Rev, 2019. **48**(12): p. 3193-3228.
2. Xu, Y., et al., *A hydrophobic FeMn@Si catalyst increases olefins from syngas by suppressing C1 by-products.* Science, 2021. **371**(6529): p. 610-613.
3. Jiao, F., et al., *Selective conversion of syngas to light olefins.* Science, 2016. **351**(6277): p. 1065-8.
4. Gholami, Z., Z. Tišler, and V. Rubáš, *Recent advances in Fischer-Tropsch synthesis using cobalt-based catalysts: a review on supports, promoters, and reactors.* Catalysis Reviews, 2020. **63**(3): p. 512-595.
5. Colley, S., et al., *Carbon monoxide hydrogenation using cobalt manganese oxide catalysts: initial catalyst optimization studies.* Industrial & Engineering Chemistry Research, 2002. **27**(8): p. 1339-1344.
6. F. Morales Cano, O.L.J.G., F.M.F. de Groot, B.M. Weckhuysen, *Manganese promotion in cobalt-based Fischer-Tropsch catalysis.* Studies in Surface Science and Catalysis, 2004. **147**: p. 271-276.
7. Morales, F., et al., *In Situ X-ray Absorption of Co/Mn/TiO2 Catalysts for Fischer–Tropsch Synthesis.* The Journal of Physical Chemistry B, 2004. **108**(41): p. 16201-16207.
8. Keyser, M.J., R.C. Everson, and R.L. Espinoza, *Fischer–Tropsch Kinetic Studies with Cobalt–Manganese Oxide Catalysts.* Industrial & Engineering Chemistry Research, 1999. **39**(1): p. 48-54.
9. Atashi, H., et al., *Kinetic study of Fischer–Tropsch process on titania-supported cobalt–manganese catalyst.* Journal of Industrial and Engineering Chemistry, 2010. **16**(6): p. 952-961.
10. Dinse, A., et al., *Effects of Mn promotion on the activity and selectivity of Co/SiO2 for Fischer–Tropsch Synthesis.* Journal of Catalysis, 2012. **288**: p. 104-114.
11. Werner, S., G.R. Johnson, and A.T. Bell, *Synthesis and Characterization of Supported Cobalt-Manganese Nanoparticles as Model Catalysts for Fischer-Tropsch Synthesis.* ChemCatChem, 2014. **6**(10): p. 2881-2888.
12. Johnson, G.R., S. Werner, and A.T. Bell, *An Investigation into the Effects of Mn Promotion on the Activity and Selectivity of Co/SiO2 for Fischer–Tropsch Synthesis: Evidence for Enhanced CO Adsorption and Dissociation.* ACS Catalysis, 2015. **5**(10): p. 5888-5903.

13. Johnson, G.R., et al., *Investigations of element spatial correlation in Mn-promoted Co-based Fischer–Tropsch synthesis catalysts.* Journal of Catalysis, 2015. **328**: p. 111-122.

14. Johnson, G.R. and A.T. Bell, *Effects of Lewis acidity of metal oxide promoters on the activity and selectivity of Co-based Fischer–Tropsch synthesis catalysts.* Journal of Catalysis, 2016. **338**: p. 250-264.

15. Koshy, D.M., et al., *Scanning Nanobeam Diffraction and Energy Dispersive Spectroscopy Characterization of a Model Mn-Promoted Co/Al2O3 Nanosphere Catalyst for Fischer–Tropsch Synthesis.* ACS Catalysis, 2020. **10**(20): p. 12071-12079.

16. Xiang, Y., L. Kovarik, and N. Kruse, *Rate and selectivity hysteresis during the carbon monoxide hydrogenation over promoted Co/MnOx catalysts.* Nat Commun, 2019. **10**(1): p. 3953.

17. Schröder, D., et al., *Influence of the formation of short-chain olefins by manganese/cobalt-catalyzed Fischer–Tropsch synthesis on the selectivity and effective reaction rate.* Catalysis Science & Technology, 2020. **10**(2): p. 475-483.

18. Voss, J.M., et al., *Characterization of CoCu- and CoMn-Based Catalysts for the Fischer–Tropsch Reaction Toward Chain-Lengthened Oxygenates.* Topics in Catalysis, 2018. **61**(9-11): p. 1016-1023.

19. Xiang, Y. and N. Kruse, *Tuning the catalytic CO hydrogenation to straight- and long-chain aldehydes/alcohols and olefins/paraffins.* Nat Commun, 2016. **7**: p. 13058.

20. Athariboroujeny, M., et al., *Competing Mechanisms in CO Hydrogenation over Co-MnOx Catalysts.* ACS Catalysis, 2019. **9**(6): p. 5603-5612.

21. Zhong, L., et al., *Cobalt carbide nanoprisms for direct production of lower olefins from syngas.* Nature, 2016. **538**(7623): p. 84-87.

22. Lin, T., et al., *Cobalt Carbide Nanocatalysts for Efficient Syngas Conversion to Value-Added Chemicals with High Selectivity.* Acc Chem Res, 2021. **54**(8): p. 1961-1971.

23. Ertl, G. and H.J. Freund, *Catalysis and surface science.* Physics Today, 1999. **52**(1): p. 32-38.

24. Musselwhite, N. and G.A. Somorjai, *Investigations of Structure Sensitivity in Heterogeneous Catalysis: From Single Crystals to Monodisperse Nanoparticles.* Topics in Catalysis, 2013. **56**(15-17): p. 1277-1283.

25. Tuxen, A., et al., *Size-dependent dissociation of carbon monoxide on cobalt nanoparticles.* J Am Chem Soc, 2013. **135**(6): p. 2273-8.

26. Puntes, V.F., K.M. Krishnan, and A.P. Alivisatos, *Colloidal Nanocrystal Shape and Size Control: The Case of Cobalt.* Science, 2001. **291**(5511): p. 2115-2117.

27. Carenco, S., et al., *Dealloying of Cobalt from CuCo Nanoparticles under Syngas Exposure.* The Journal of Physical Chemistry C, 2013. **117**(12): p. 6259-6266.

28. Wu, C.H., et al., *Ambient-Pressure X-ray Photoelectron Spectroscopy Study of Cobalt Foil Model Catalyst under CO, H2, and Their Mixtures.* ACS Catalysis, 2017. **7**(2): p. 1150-1157.

29. Escudero, C., et al., *A reaction cell with sample laser heating for in situ soft X-ray absorption spectroscopy studies under environmental conditions.* J Synchrotron Radiat, 2013. **20**(Pt 3): p. 504-8.

30. Frati, F., M. Hunault, and F.M.F. de Groot, *Oxygen K-edge X-ray Absorption Spectra.* Chem Rev, 2020. **120**(9): p. 4056-4110.

31. Salmeron, M. and G.A. Somorjai, *Desorption, decomposition, and deuterium exchange reactions of unsaturated hydrocarbons (ethylene, acetylene, propylene, and butenes) on the platinum(111) crystal face.* The Journal of Physical Chemistry, 1982. **86**(3): p. 341-350.

32. Tsai, Y.-L., C. Xu, and B.E. Koel, *Chemisorption of ethylene, propylene and isobutylene on ordered Sn/Pt(111) surface alloys.* Surface Science, 1997. **385**(1): p. 37-59.

33. Álvarez-Moreno, M., et al., *Managing the Computational Chemistry Big Data Problem: The ioChem-BD Platform.* Journal of Chemical Information and Modeling, 2015. **55**(1): p. 95-103.